Design principles for transporting vesicles with enclosed active particles

SARVESH UPLAP, MICHAEL F. HAGAN* and APARNA BASKARAN*

Martin Fisher School of Physics, Brandeis University, 415 South Street, Waltham, Massachusetts 02453, USA *hagan@brandeis.edu, aparna@brandeis.edu

*** Missing PACS ***

Abstract – We use coarse-grained molecular dynamics simulations to study the motility of a 2D vesicle containing self-propelled rods, as a function of the vesicle bending rigidity and the number density, length, and activity of the enclosed rods. Above a threshold value of the rod length, distinct dynamical regimes emerge, including a dramatic enhancement of vesicle motility characterized by a highly persistent random walk. These regimes are determined by the clustering of the rods within the vesicle; the maximum motility state arises when there is one long-lived polar cluster. We develop a scaling theory that predicts the dynamical regimes as a function of control parameters and shows that feedback between activity and passive membrane forces govern the rod organization. These findings yield design principles for building self-propelled superstructures using independent active agents under deformable confinement.

Introduction. — Interacting systems of minimal motile agents occur on diverse length scales in biology, from the molecular motors and filaments in the cytoskeleton of the cell [1, 2] to insect colonies [3–5] and animal herds [6–8]. The emergent behaviors exhibited by these systems have been extensively studied within the paradigm of active matter [9–14]. In parallel, the same phenomena have inspired the field of collective robotics and swarm intelligence [15–18], where it has been recognized that collective efforts of simple agents yield robust and adaptable emergent behaviors that can be harnessed for specific tasks. Recent realizations of collective robotics have been used for programmable self—assembly [19–22], mimicking the foraging behavior of insects [23, 24], and sentry duties over unmapped and variable terrains [25].

Physical interactions between motile agents will inevitably affect their collective behaviors. To successfully use minimally programmed agents to perform specific tasks, and to build small-scale soft robotic systems, we should leverage physical interactions as a design and control asset rather than a bottleneck that needs to be eliminated by programming or material design. Knowledge and models from statistical and soft matter physics can play important roles in this context. To that end, we consider a minimal example of collective behavior of motile agents — self-propelled (active) agents confined in an elastic vesicle. The specific function we consider is the

transport of the vesicle, and we identify the role played by physical interactions in aiding or hindering this task.

Collections of confined active agents form transient clusters that push against their boundaries [26–33]. When confined to deformable boundaries, spontaneous fluctuations can result in the boundary developing large curvatures and spontaneous motion of the entire system [34–40]. The benefit of such transient assemblies was demonstrated for a system of small simple robots confined by a flexible mobile enclosure [41]. It was shown that aggregation of the robots led to transient directed motion in random directions and that the small robots can transport the enclosing frame around obstacles and through narrow openings, much like a collection of ants can manipulate large food items [42, 43]. However, to leverage this basic physics to build a robust collective robotic system, we must understand how spontaneous fluctuations can be preferentially biased and rectified so as to predominantly aid in the desired transport.

In this paper, we employ Langevin dynamics simulations to study the transport of a 2D elastic vesicle, by self-organization of self-propelled rods enclosed within it. The entire system is on a frictional substrate that provides a momentum sink to both the particles and the vesicle. This basic phenomenology has been demonstrated in the literature [40]. We build on this work by considering a minimal model for the enclosed rods, which enables us

to identify physical relationships between vesicle and rod properties that control the emergent phenomenology. We find that the rods spontaneously form clusters or caps on the vesicle boundary, and under certain conditions, the rods form a single polar cap which leads to highly efficient directed motion of the vesicle and its contents. However, under other conditions the rods form multiple caps whose self-propulsion forces partially cancel, hindering motility. Analysis shows that the cap organization is determined by cooperative feedback between effective rod-rod attractions arising from their self-propulsion, the active forces of rods pushing on the vesicle boundary, and the passive reaction force from the deformed vesicle. We present simple scaling arguments that capture many of the observations from the simulations, and thereby identify optimal design principles for maximizing the vesicle motility.

Model. — We perform Langevin dynamics simulations in 2D of $N_{\rm rods}$ self-propelled, rigid rods enclosed by a passive elastic vesicle, which is represented as a semiflexible bead-spring ring polymer. Details of the microscopic model are as follows.

Self-propelled rods: Each rod consists of n+1 beads of diameter σ , with the centers of neighboring beads separated by a distance $b=0.5\sigma$ so that the rod length is $\ell=nb+\sigma$. Overlapping beads in this manner reduces surface roughness, thereby preventing interlocking of rods at high density [30, 44, 45]. The central bead is subjected to a constant self-propulsion force of magnitude $f_{\rm a}$ along the rod axis, characterized by an orientation vector $\hat{\nu}=(\cos\theta,\sin\theta)$, where θ is the angle of the rod axis with the x direction in the lab frame. Each rod bead interacts with all beads on other rods and the vesicle through a force-shifted WCA potential, $U_{\rm WCA}=4\epsilon\left[\left(\frac{\sigma}{r}\right)^{12}-\left(\frac{\sigma}{r}\right)^6\right]+\Delta V$, for interparticle distances $r< r_{\rm cut}$ and zero otherwise [46, 47]. The potential is cutoff at the Lennard-Jones minimum distance $r_{\rm cut}=2^{1/6}\sigma$, and the repulsion strength is set to $\epsilon=k_{\rm B}T$.

The mass of the central bead, which is set to m=1, sets the total rod mass. The equations of motion are integrated for the central bead of each rod only (the rods move as rigid bodies), with the forces \bar{F}^{rigid} and torques T^{rigid} from the constituent particles transferred to the central bead. The equations of motion for the i^{th} rod are:

$$\xi^{\mathrm{T}} \frac{d\bar{r}_i}{dt} = f_{\mathrm{a}} \hat{\nu} + \bar{F}_i^{\mathrm{rigid}} + \bar{\eta}_i^{\mathrm{T}}(t)$$
 (1)

$$\xi^{R} \frac{d\theta_{i}}{dt} = T_{i}^{\text{rigid}} + \eta_{i}^{R}(t) \tag{2}$$

$$\bar{F}_{i}^{\text{rigid}} = -\sum_{j \neq i}^{N_{\text{rods}}} \sum_{m,m'=1}^{n} \nabla_{\bar{r}_{i}} U_{\text{WCA}} \left(|\bar{r}_{i,m} - \bar{r}_{j,m'}| \right)$$

$$-\sum_{k=1}^{N_{\text{ves}}} \sum_{m=1}^{n} \nabla_{\bar{r}_{i}} U_{\text{WCA}} \left(|\bar{r}_{i,m} - \bar{r}_{k}| \right) \tag{S}$$

where $\xi^{\rm T}$ and $\xi^{\rm R}$ are the translational and rotational drag coefficients for the rods; $\bar{\eta}_i^{\rm T}$, $\eta_i^{\rm R}$ are uniform random forces modelled as Gaussian white noise with moments $\langle \bar{\eta}_i^{\rm T}(t) \rangle = 0$, $\langle \eta_i^{\rm R}(t) \rangle = 0$ and $\langle \bar{\eta}_i^{\rm T}(t) \cdot \bar{\eta}_j^{\rm T}(t') \rangle = 4k_{\rm B}T\xi^{\rm T}\delta_{ij}\delta(t-t')$; and $\langle \eta_i^{\rm R}(t)\eta_j^{\rm R}(t') \rangle = 2k_{\rm B}T\xi^{\rm R}\delta_{ij}\delta(t-t')$. In Eq. (3), $\bar{r}_{i,m}$ is the position of bead m on rod i, and \bar{r}_k is the position of vesicle bead k. The torque $T_i^{\rm rigid}$ is computed from the forces on each bead in rod i. Because the rod motions are dominated by active rather than thermal effects, and to distinguish effects of propulsion and sterics, we set the rod active force f_a and friction constants to be independent of rod length. The latter are set to $\xi^{\rm T}=10\xi_0$ and $\xi^{\rm R}=1000\sigma^2\xi_0$, with ξ_0 the friction coefficient for a bead with diameter σ .

Elastic vesicle: We model the vesicle as a passive semiflexible bead-spring ring polymer. The total interaction potential for the vesicle is given by $U_{\text{ves}} = \sum_{i=1}^{N_{\text{ves}}} U_{\text{stretch}}(r_{ii+1}) + \sum_{i=2}^{N_{\text{ves}}-1} U_{\text{bend}}(\phi_{i-1,i,i+1}) + \sum_{\langle ij \rangle} U_{\text{WCA}}(r_{ij})$, where $r_{ij} \equiv |\bar{r}_i - \bar{r}_j|$; stretching penalties are enforced by harmonic bonds between neighboring beads, $U_{\text{stretch}}(r) = \kappa_{\text{S}}(r-b)^2$ with κ_{S} the stretching modulus; the bending energy is given by $U_{\text{bend}}(\phi) = \kappa_{\text{B}}'(\pi-\phi)^2$, with ϕ the angle made by three consecutive beads (or two consecutive bonds). The continuum bending modulus is $\kappa_{\text{B}} = 2b\kappa_{\text{B}}'$ and thus $\kappa_{\text{B}} = \kappa_{\text{B}}'\sigma$ for our parameters. The non-bonded interaction is given by the WCA potential and is summed over all vesicle-rod pairs of beads. The equation of motion for the i^{th} vesicle bead is:

$$\frac{d^2\bar{r}_i}{dt^2} = -\xi_V \frac{d\bar{r}_i}{dt} - \nabla_{\bar{r}_i} U_{\text{ves}} + \bar{\eta}_i^{\text{ves}}(t) \tag{4}$$

where $\xi_{\rm V}=\xi_0$ is the translational drag coefficient and $\bar{\eta}_i^{\rm ves}$ is Gaussian white noise representing thermal motion. The moments of the thermal noise are $\langle \bar{\eta}_i^{\rm ves}(t) \rangle = 0$ and $\langle \bar{\eta}_i^{\rm ves}(t) \cdot \bar{\eta}_j^{\rm ves}(t') \rangle = 4k_{\rm B}T\xi_{\rm V}\delta_{ij}\delta(t-t')$. The mass of each vesicle bead is set to m=1. For all results reported in this work the vesicle comprises $N_{\rm ves}=1005$ beads so that the equilibrium vesicle radius is $R_{\rm ves}=80\sigma$. Further, we set $\kappa_{\rm S}=5\times 10^5k_{\rm B}T$ and vary $\kappa_{\rm B}$ over the range $[1k_{\rm B}T\sigma..10^6k_{\rm B}T\sigma]$. While we simulate rod motions with overdamped Brownian dynamics due to their large size, we employ Langevin dynamics for the vesicle beads to allow for possible effects of inertia. We present all results in units of $\tau_{\rm s}=\sigma^2\xi_0/k_{\rm B}T$, the diffusive timescale for a bead with the diameter of a rod.

Results. –

Phenomenology of vesicle motion. Our goal is to characterize the motility of the vesicle. We begin by focusing on its center of mass, $\bar{r}(t)$. We find that the dynamics of $\bar{r}(t)$ is well described by a persistent random walk with $\langle |\bar{r}(t) - \bar{r}(t + \Delta t)|^2 \rangle = D[\Delta t - \lambda + \lambda e^{-\Delta t/\lambda}]$, where λ is the persistence time and D is the diffusion coefficient describing the vesicle motions at times $t \gg \lambda$ (Fig. 1a). Further, we measure $\bar{F}_{\rm net}$, the net active force on the vesicle, exerted by the enclosed rods that are in contact with it and $\bar{v}_{\rm com}$, the center of mass velocity. We find that both quantities are distributed normally (Fig. 1b) and exponentially

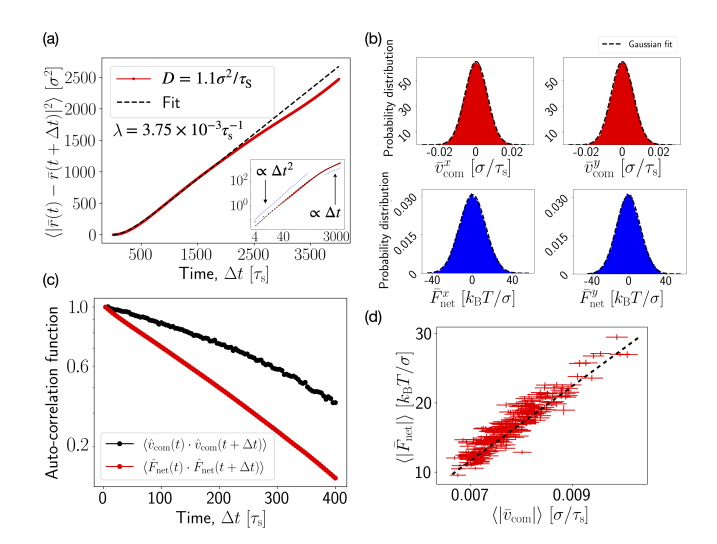


Fig. 1: Statistical properties of the center-of-mass motion of a vesicle with bending modulus $\kappa_{\rm B} = 3000k_{\rm B}T$ containing $N_{\rm rods} = 30$ rods of aspect ratio $\ell/\sigma = 3$ with active force $f_{\rm a} = 3k_{\rm B}T/\sigma$. (a) The mean square displacement (MSD) of the center of mass, fit to the functional form of persistent random walk to obtain the translational diffusion coefficient D. Inset: Same data shown in log-log scale. The dashed lines indicate scaling consistent with ballistic/diffusive dynamics at short/long times. The MSDs were measured from simulation times $t/\tau >= 5000$ from 100 independent trials at each parameter set. (b) The probability distributions of x and ycomponents of the net force $\bar{F}_{\rm net}$ and center-of-mass velocity $\bar{v}_{\rm com}$. The distributions are Gaussian with zero mean. (c) Autocorrelation functions for the net force and velocity, $\langle \hat{F}_{\text{net}}(t) \cdot \hat{F}_{\text{net}}(t + \Delta t) \rangle$ and $\langle \hat{v}_{\text{com}}(t) \cdot \hat{v}_{\text{com}}(t + \Delta t) \rangle$. The correlation times $\lambda_{\rm v}$ and $\lambda_{\rm f}$ are extracted by fitting these measurements to exponentials. (d) Plot of the mean active force $\langle |\bar{F}_{\rm net}| \rangle$ against the mean velocity $\langle |\bar{v}_{\rm com}| \rangle$, showing they are highly correlated. Timescales are reported in units of τ_s , the time for one bead to diffuse a distance of its diameter.

correlated in time (Fig. 1c), while being proportional to each other instantaneously (Fig. 1d). While it is suggestive to map the emergent persistent random walk of our vesicle to the well-studied Active Brownian Particle model [12,48], we find that the dynamics is more complex due to timescales arising from reorganization of the enclosed rods. Therefore, as we vary the physical properties of the vesicle building blocks, we characterize its motility by the diffusion coefficient D, and the correlation times of the velocity and the force, $\lambda_{\rm v}$ and $\lambda_{\rm f}$ respectively (further information in SI section IIF).

Dependence of motility on vesicle stiffness and active rod length. To highlight the key findings of this study, let us consider the physics we know from prior studies on self-propelled particles at curved walls [32,35–37,37,38,49,50]. Self-propelled particles cluster at walls [26,27,29,30,51], and tend to accumulate in regions of high curvature [32,49,52–54]. This can lead to spontaneous motion of rigid containers [55–57]. Since our vesicle is deformable

in the present work, we expect curvature to increase in regions of accumulation and thereby lead to recruitment of more particles into the cap [34–38,40,41,54]. This feedback mechanism should be greater for vesicles with lower bending rigidity, since the curvature amplification will be larger for a given active force magnitude and local particle density. Thus, we might naively expect softer vesicles to have higher motility compared to stiff ones, since they provide a pathway to the formation of a few larger caps rather than a more uniform distribution of particles along the boundary.

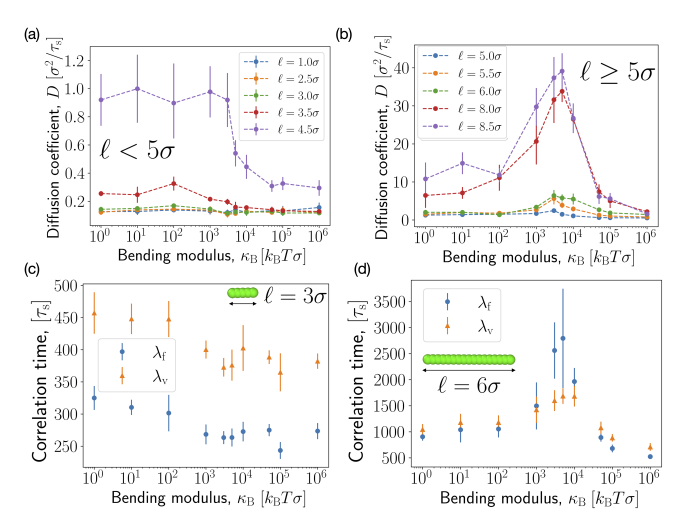


Fig. 2: (a,b) Dependence of the vesicle diffusion constant on the vesicle bending modulus $\kappa_{\rm B}$ for indicated values of the rod aspect ratio ℓ/σ , for aspect ratios that are (a) below the threshold for long-lived caps ($\ell/\sigma < 5$) and (b) above the threshold ($\ell/\sigma \geq 5$). (c,d) The correlation times of the net force and the center-of-mass velocity for (c) below threshold aspect ratio ($\ell/\sigma = 3$), showing that both are independent of vesicle stiffness, and (d) above threshold ($\ell/\sigma = 6$) showing enhanced correlation at the optimal stiffness.

Our first observation is that this simple argument is not the full story. Fig. 2 characterizes the vesicle motility for fixed $N_{\rm rods}=30$ rods and activity $f_{\rm a}=3k_{\rm B}T/\sigma$ as a function of the rod aspect ratio ℓ/σ and vesicle stiffness $\kappa_{\rm B}$. We identify three distinct behaviors: (i) for $\ell/\sigma \leq 3$, the motility is independent of vesicle bending stiffness, (ii) for $3<\ell/\sigma \leq 5$, the motility increases as the vesicle softens, and (iii) for longer rods a strong non-monotonic dependence on stiffness emerges.

We can understand these changes in phenomenology as a function of aspect ratio by considering the limiting case of $\ell/\sigma=1$, i.e., spheres, in an infinitely stiff, i.e., rigid, circular vesicle. Supposing that the system was initialized with isotropically distributed self-propulsion forces, as all the simulations in this study are, we expect a uniform distribution of particle orientations on the vesicle boundary. Therefore, the net force on the center of mass is small and its fluctuations are correlated on the same time scale as the bare correlations of isolated active particles. Hence,

the enclosed active particles will not enhance the vesicle motility to any significant degree. When we move away from the rigid limit, deformations of the vesicle do induce larger caps and appreciable density variation along the boundary. But, as $\ell/\sigma \to 1$, neither the boundary nor the inter-particle interactions can exert significant torques to realign the active forces. Thus, the net force on the vesicle remains small and enhancement of motility negligible. Given this picture, we can understand the low aspect ratio results in Fig. 2a as the generalization of this asymptotic case of spherical particles.

Now let us switch focus to the stiffness dependence of motility for longer rods. Again, it is useful to first build a heuristic based on known phenomenology [58]. Let us consider long rods accumulated at a rigid circular boundary. Suppose the rods do not interact with each other, i.e., in the dilute limit, they would slide along the boundary until they become tangential to it [11, 26, 30, 32, 49]. But, when the rods collide at the boundary, the inter-particle interactions will lead the rods to align such that they form polar caps that are normal to the boundary [11, 26, 33]. These polar caps push on the boundary, thus inducing and amplifying local curvature fluctuations when the boundary is no longer rigid. In turn, the rods' forward motion couples to the vesicle curvature to result in an effective attraction between neighboring rods. For softer vesicles, the induced curvature and corresponding effective rod-rod attraction increases, thus resulting in larger and longer-lived polar caps. For moderate aspect-ratio rods, this effect leads to an increase in vesicle motility with decreasing vesicle rigidity (most easily seen in Fig. 2a for $\ell/\sigma = 4.5$). However, for longer rods, this phenomenology is overwhelmed by the emergence of an optimal stiffness, around which there is a huge enhancement of motility above the basic trend (see Fig. 2 (b,d)).

To elucidate the mechanism underlying the dramatic motility enhancement for optimal vesicle stiffness, we now examine the organization of active rods within the vesicle (Fig. 3). We find that the enhanced motility states are characterized by the presence of a single (Fig. 3a) longlived (SI Fig. 5) polar cluster of rods. Hence, essentially all encapsulated rods point in the same direction, leading to a large net active force on the vesicle $\bar{F}_{\rm net} \sim f_{\rm a} N_{\rm rods}$ and correspondingly a large persistence length for the vesicle's motion. For vesicles that are softer than the optimal stiffness, the rods organize into two or more polar caps. Through the combination of the caps's polar motion and the consequent local curvature of the membrane, there is an effective repulsion between caps driving them into a steady-state configuration in which their active forces tend to cancel (see Fig. 3c, Fig. 5a, and SI section I). Consequently, the vesicle exhibits a much smaller persistence length than for the 1-cap state. For stiffer-thanoptimal vesicles, the rods can only weakly deform the vesicle boundary. Since local curvature of the vesicle is essential to stabilize the polar cap (see below), only transient caps form. Therefore, the direction of $\bar{F}_{\rm net}$ fluctuates rapidly and the vesicle motion is characterized by a small persistence length. These observations suggest that both the aligning interactions among the rods due to their self-propulsion and the vesicle deformability are crucial to the emergence of the enhanced motility states. As evidence of the importance of direct rod-rod alignment interactions, we observe large net active forces on the vesicle only for large aspect-ratio rods (Fig. 3b).

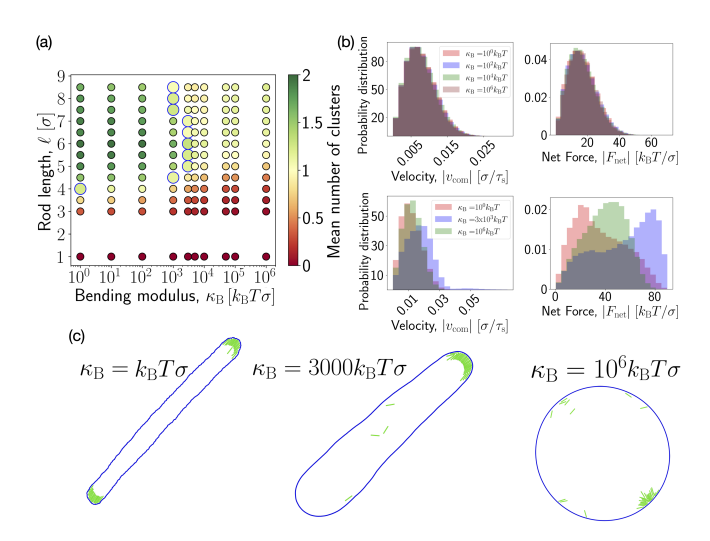
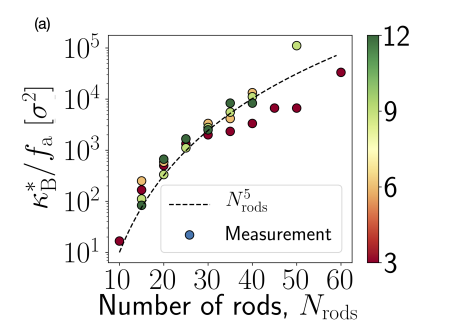


Fig. 3: (a) Mean number of caps as a function of rod aspect ratio and vesicle bending modulus for active force $f_{\rm a}=3k_{\rm B}T/\sigma$. A single long-lived cap emerges at the optimal value of stiffness, $\kappa_{\rm B}\approx 3000k_{\rm B}T$. The optimal stiffness for each aspect ratio is indicated by an enlarged marker. (b) Probability distributions of $\bar{F}_{\rm net}$ and $\bar{v}_{\rm com}$ for (top) $\ell/\sigma=3$ and (bottom) $\ell/\sigma=6$, showing that the net force shifts to large values at the optimal stiffness for long rods. (c) Snapshots illustrating the rod organization for $\ell/\sigma=6$ for (left) low, (middle) optimal, and (right) high bending modulus.

Assembly principles for the single cap state. Now, we seek to quantify the emergence of a single cap in terms of the physical parameters of the building blocks of our motile vesicle. As we have shown in previous work [33], long-lived caps can be fruitfully described as self-limited structures whose size can be accurately captured using the concepts of self-assembly. We lay out below a physical description of the model that predicts the number and sizes of caps as a function of parameters, and we use these estimates to predict the optimal stiffness at which the huge enhancement in motility occurs. The mathematical details are given in SI Section I.

We know from previous work that self-propulsion together with the presence of the wall drives rods to align with each other, perpendicular to the wall, and to maximize the overlap along their length with their neighbors. That is, the rods tend to form smectic layers at the wall [58]. We can capture this phenomenology through an effective 'energy' of the form $U_{\text{active}} + U_{\text{interfacial}}$, where $U_{\text{active}} = -C\sigma f_{\text{a}} n_{\text{r}}$, an attractive interaction that scales with the activity and number of rods in the cap n_{r} , and



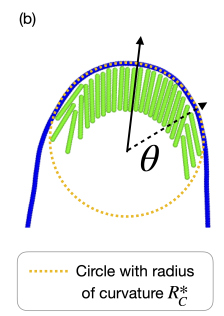


Fig. 4: (a) Comparison of the theoretical scaling of the optimal bending modulus with the number of enclosed rods and active force, $\kappa_{\rm B}^*/f_{\rm a} \sim N_{\rm rods}^5$, with measurements from the simulations. (b) Schematic showing a visual representation of the angular size θ of a cap, with θ measured from the center of the cap.

 $U_{\rm interfacial} = -2\gamma$ is a surface tension that accounts for the absence of neighbors at either edge of a cap. The surface tension encodes the tendency for caps to grow. While this captures the phenomenology at a flat wall, the curvature of the vesicle 'opposes' the growth of the cap by forcing rods within a cap to shear relative to their neighbors, thus preventing the perfect overlap that flat walls would allow. We can capture this effect through an energy $U_{\rm shear} = -2k_{\rm shear}\log(\cos\theta)$, where θ is the angular extent of the cap (see Fig. 4b) and the constant $k_{\rm shear}$ also scales with activity $f_{\rm a}$, consistent with the attractive interactions that lead to the clustering.

For a given cap size, the angular extent of a cap depends on the local radius of curvature of the vesicle, which is determined by a balance of active force of the rods and the elastic response of the vesicle. We describe this phenomenology through an energy $U_{\rm ves} = U_{\rm bend} + U_{\rm f}$, where $U_{\rm bend}$ is the standard Helfrich free energy [59–61] and $U_{\rm f} = -f_{\rm a} n_{\rm r} l$ is the work done by the active force (see SI Section I). Putting all this together, the number and size of caps, and correspondingly the steady-state geometry of the vesicle, can be described by finding the minimum of a free energy of the form $U(\kappa_{\rm B}, f_{\rm a}, N_{\rm rods}) = U_{\rm rods} + U_{\rm ves}$, where $U_{\rm rods} = U_{\rm active} + U_{\rm interfacial} + U_{\rm shear}$, described above.

In particular, the analysis shows that, starting from the floppy vesicle limit $\kappa_{\rm B} \to 0$, the number of stable caps decreases with increasing bending modulus. By calculating when the system transitions from a two-cap state to a single cap state, corresponding to the highly motile states observed in the simulations, we can estimate that the optimal stiffness scales as $\kappa_{\rm B}^*/f_{\rm a} \sim N_{\rm rods}^5$ (see Eq. 20 in section ID of the SI). The predicted scaling with both activity and number of enclosed rods shows good agreement with our simulation results (Fig. 4a), although the accessible range of $N_{\rm rods}$ within the vesicle size that we focus on $(R_{\rm ves}=80\sigma)$ is insufficient to rigorously test the scaling exponent.

The analysis predicts that this trend continues until a threshold value of the bending modulus $\kappa_{\rm B}^{\rm max} \sim R_{\rm ves}^2 f_{\rm a}$, above which the active force is insufficient to deform the

membrane. Because membrane deformation is essential to stabilize long-lived polar caps, we expect only transient caps for stiffer vesicles. Furthermore, equating this limit with the transition value for the single cap state, i.e. $\kappa_{\rm B}^* = \kappa_{\rm B}^{\rm max}$, identifies a maximum number of enclosed rods $N_{\rm rods}^{\rm max} \sim (R_{\rm ves}\ell)^{2/5}$ above which the system will transition directly from multiple-cap states to transient caps with increasing bending modulus. Thus, for $N_{\rm rods} > N_{\rm rods}^{\rm max}$ the system will not exhibit the single-cap high-motility state for any parameter values. For our vesicle size $R_{\rm ves} = 80\sigma$ and the range of aspect-ratios that lead to polar caps $(\ell/\sigma \geq 6)$ this estimates $N_{\rm rods}^{\rm max}$ is order 10 to within a scaling constant, which is consistent with the simulation results that we do not observe the single-cap state for $N_{\rm rods} \gtrsim 60$

Since the number of caps is closely linked to the steadystate geometry of the vesicle configuration (see Fig. 5), further analysis of this theoretical model can be leveraged to design shapes of 2D active vesicles (similar to [33,54]). We defer this to future work, in order to keep the focus of this article on motility of the vesicle.

Dependence of rod organization and vesicle motility on number of enclosed rods. The scaling relationship above provides a quantitative design principle for building highly motile vesicles. But one important limitation it identifies is that motility enhancement through the formation of the single cap state only applies in the dilute limit. This corresponds to $N_{\rm rods} < N_{\rm rods}^{\rm max} \approx 60$ for the vesicle size that we focus on $R_{\rm ves} = 80\sigma$. Above this limit, there are too many rods to form a state in which there is a single polar-aligned cap. Consequently, the simple picture of three distinct dynamical regimes for large aspect-ratio rods $(\ell > 5\sigma)$ breaks down (Fig. 5).

Fig. 5a is a visual representation of the structures formed by the enclosed rods as the number of rods increases. In the intermediate regime, (60 $\lesssim N_{\rm rods} \lesssim 100$ for $R_{\text{ves}} = 80\sigma$), the dominant steady-state configurations gradually shift from 2-cap to 3-cap states with increasing $N_{\rm rods}$ in floppy vesicles, 1-cap to 2-cap states for intermediate stiffness, and one or more transient caps at high vesicle stiffness. However, even though self-limited caps continue to form in softer vesicles, the caps lack perfect polar alignment and tend to become multilayered. We speculate that this phenomenology reflects the onset of motility induced phase separation (MIPS) related behaviors at these densities [58, 62–64], which unevenly and transiently enhance clustering. At higher densities $(N_{\rm rods} > 100 \text{ for})$ $R_{\rm ves} = 80\sigma$ and $f_{\rm a} = 3k_{\rm B}T/\sigma$), the MIPS dominates the organization of the self-propelled rods at the boundary. In this regime, the rods tend to form aggregates comprising multiple sub-clusters with different orientations. For example, in floppy vesicles, the dominant rod organization corresponds to three aggregates sitting at three vertices of a triangular configuration. As noted above, the combination of rod-propulsion and membrane-curvature-mediated interactions tends to drive caps away from each other, sta-

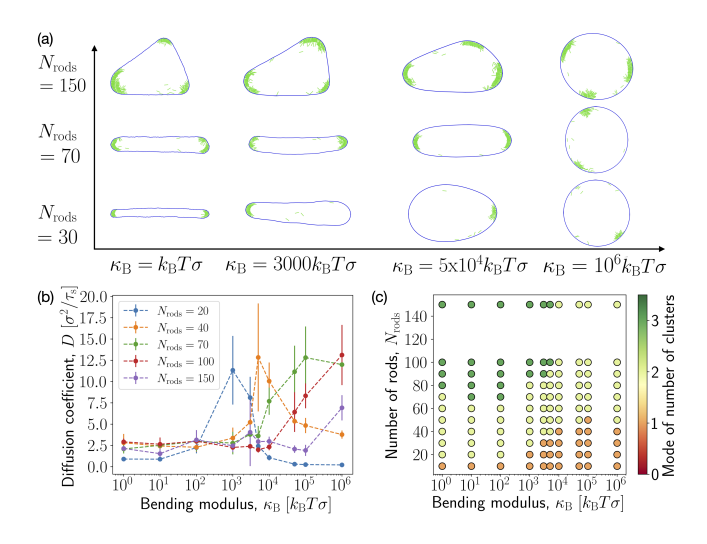


Fig. 5: (a) Snapshots of states that typify the dominant cap configurations as a function of number of enclosed rods $N_{\rm rods}$ and vesicle bending modulus. (b) The vesicle diffusion coefficient as a function of bending modulus for indicated $N_{\rm rods}$. (c) The mode of the number of caps within a vesicle as a function of bending modulus and $N_{\rm rods}$, showing that the single-cap state is not observed for $N_{\rm rods}\gtrsim 60$ enclosed rods. Results are shown for $f_{\rm a}=3k_{\rm B}T/\sigma$ and $\ell/\sigma=10$.

bilizing the triangular arrangement. However, because the rods within a given aggregate are not all aligned, aggregates are transient, tending to break apart and merge with other aggregates. With increasing $\kappa_{\rm B}$ the mean number of caps decreases, but the caps remain transient and thus do not lead to the highly motile vesicle dynamics characterized by a long persistence length. Furthermore, even in the 1-cap states at these higher rod densities, there are additional rods forming transient caps elsewhere on the boundary, which have orientations for which the propulsion forces partly cancel those of the rods in the cap.

Fig. 5b characterizes the motility of the vesicle for different numbers of enclosed rods. For the intermediate densities, the diffusion coefficient as a function of vesicle stiffness shows similar trends as seen in Fig. 2b, with motility increasing with $\kappa_{\rm B}$ for floppy vesicles and the value of optimal stiffness $\kappa_{\rm B}^*$ shifting toward larger values with increasing number of rods. This is consistent with the fact that the number of caps decreases with stiffness, thus increasing the average magnitude of the net active force. However, the motility enhancement is significantly smaller than for $N_{\text{rods}} < N_{\text{rods}}^{\text{max}}$, due to the imperfect alignment of the caps. At higher densities ($N_{\rm rods} > 100$), the motility becomes largely independent of stiffness. This reflects the fact that, when the MIPS phenomenology dominates, the caps lack polar order and are transient. Thus, the net active force lacks the large magnitude and long-lived orientation that drive directed vesicle motion.

Summary and Outlook. – This work identifies design principles for constructing elastic vesicles with programmable classes of motilities, which range from Brown-

ian to highly persistent, by encapsulating self-propelled rods. In particular, for a given rod aspect ratio and activity level, our simple theoretical framework predicts the vesicle bending modulus and number of encapsulated agents that maximize the vesicle motility.

There is now a robust understanding of active matter phenomenology for many model systems. However, leveraging this fundamental knowledge to design architectures with specific functional goals has been relatively limited. We hope that this investigation, on the simple functional goal of emergent motility, can serve as a template for investigations into other, potentially more sophisticated functions. A direct extension of this work would be to leverage physical interactions or spatiotemporal activity to render an elastic vesicle steerable. For example, one could consider vesicles of nonuniform stiffness where cap formation occurs preferentially at certain sites, or cycling activity as a function of time. Such investigations may lead to a better understanding of how to extract function from systems of interacting motile agents.

* * *

This work was supported by the National Science Foundation (NSF) DMR-1855914 (SU and MFH), DMR-2202353 (AB) and the Brandeis Center for Bioinspired Soft Materials, an NSF MRSEC DMR-2011846 (SU, AB, and MFH). Computing resources were provided by the NSF XSEDE/ACCESS allocation MCB090163 (Stampede and Expanse) and the Brandeis HPCC which is partially supported by NSF DMR-MRSEC 2011846 and OAC-1920147.

REFERENCES

- S. Klumpp, R. Lipowsky, Proceedings of the National Academy of Sciences, 102 (2005) 17284.
- [2] K. Furuta, A. Furuta, Y. Y. Toyoshima, M. Amino, K. Oiwa, H. Kojima, Proceedings of the National Academy of Sciences, 110 (2012) 501.
- [3] GORDON, M. DEBORAH, Ants at work: how an insect society is organized (Simon and Schuster) 1999.
- [4] Costa, T. James, The other insect societies (Harvard University Press) 2006.
- [5] J. Buhl, D. J. T. Sumpter, I. D. Couzin, J. J. Hale, E. Despland, E. R. Miller, S. J. Simpson, *Science*, 312 (2006) 1402.
- [6] M. Ballerini, N. Cabibbo, R. Candelier, A. Cavagna, E. Cisbani, I. Giardina, V. Lecomte, A. Orlandi, G. Parisi, A. Procaccini, M. Viale, V. Zdravkovic, *Proceedings of the National Academy of Sci*ences, 105 (2008) 1232.
- [7] J. L. SILVERBERG, M. BIERBAUM, J. P. SETHNA, I. CO-HEN, Physical Review Letters, 110 (2013) 228701.
- [8] A. GARCIMARTÍN, J. M. PASTOR, L. M. FERRER, J. J. RAMOS, C. MARTÍN-GÓMEZ, I. ZURIGUEL, *Phys. Rev. E*, 91 (2015) 022808.
- [9] RAMASWAMY S., Annual Review of Condensed Matter Physics, 1 (2010) 323.

- [10] M. C. MARCHETTI, J. F. JOANNY, S. RAMASWAMY, T. B. LIVERPOOL, J. PROST, MADAN RAO, R. ADITI SIMHA, Reviews of Modern Physics, 85 (2013) 1143.
- [11] C. BECHINGER, R. D. LEONARDO, H. LÖWEN, C. RE-ICHHARDT, G. VOLPE, G. VOLPE, Reviews of Modern Physics, 88 (2016) 045006.
- [12] C. MARCHETTI, Y. FILY, S. HENKES, A. PATCH, D. YL-LANES, Current Opinion in Colloid & Interface Science, 21 (2016) 34.
- [13] M. Cates, J. Tailleur, Annual Review of Condensed Matter Physics, 6 (2015) 219.
- [14] T. Vicsek, A. Zafeiris, *Physics Reports*, **517** (2012) 71.
- [15] O. HOLLAND C. MELHUISH, Artificial Life, 5 (1999) 173.
- [16] H. Hamann, Swarm Robotics: A Formal Approach (Springer International Publishing) 2018.
- [17] Y. TAN, (Editor) Handbook of Research on Design, Control, and Modeling of Swarm Robotics (IGI Global) 2016.
- [18] S. Kernbach, (Editor) Handbook of Collective Robotics (Jenny Stanford Publishing) 2013.
- [19] M. Rubenstein, A. Cornejo, R. Nagpal, Science, 345 (2014) 795.
- [20] R. GRO, M. BONANI, F. MONDADA, M. DORIGO, IEEE Transactions on Robotics, 22 (2006) 1115.
- [21] M. YIM, W. SHEN, B. SALEMI, D. RUS, M. MOLL, H. LIPSON, E. KLAVINS, G. CHIRIKJIAN, *IEEE Robotics & Automation Magazine*, **14** (2007) 43.
- [22] S.C. GOLDSTEIN, J.D. CAMPBELL, T.C. MOWRY, Computer, 38 (2005) 99.
- [23] VAUGHAN, ADAM LEIN1 RICHARD T, Artificial Life, 11 (2008) 337.
- [24] L. E. PARKER, D. RUS, G. S. SUKHATME, Multiple mobile robot systems in Springer Handbook of Robotics (Springer International Publishing) 2016 pp. 1335–1384.
- [25] K. KONOLIGE, D. FOX, C. ORTIZ, A. AGNO, M. ERIK-SEN, B. LIMKETKAI, J. KO, B. MORISSET, D. SCHULZ, B. STEWART, R. VINCENT, Centibots: Very large scale distributed robotic teams in Springer Tracts in Advanced Robotics (Springer Berlin Heidelberg) 2006 pp. 131–140.
- [26] H. H. WENSINK, H. LÖWEN, Phys. Rev. E, 78 (2008) 031409.
- [27] X. YANG, L. M. MANNING, C. M. MARCHETTI, Soft Matter, 10 (2014) 6477.
- [28] C. F. Lee, New Journal of Physics, 15 (2013) 055007.
- [29] J. ELGETI, G. GOMPPER, EPL (Europhysics Letters), 85 (2009) 38002.
- [30] J. Elgeti, G. Gompper, EPL (Europhysics Letters), 101 (2013) 48003.
- [31] L. CAPRINI, U. M. B. MARCONI, Soft Matter, 14 (2018) 9044.
- [32] Y. FILY, A. BASKARAN, M. F. HAGAN, Physical Review E, 91 (2015) 012125.
- [33] M. S. E. Peterson, A. Baskaran, M. F. Hagan, Nature Communications, 12 (2021).
- [34] G. KOKOT, H. A. FAIZI, G. E. PRADILLO, A. SNEZHKO, P. M. VLAHOVSKA, Communications Physics, 5 (2022).
- [35] M. PAOLUZZI, R. D. LEONARDO, C. M. MARCHETTI, L. ANGELANI, Scientific Reports, 6 (2016) 34146.
- [36] W. Tian, Y. Gu, Y. Guo, K. Chen, Chinese Physics B, 26 (2017) 100502.
- [37] Y. LI, P. R. TEN WOLDE, Physical Review Letters, 123 (2019) 148003.
- [38] C. WANG, Y. GUO, W. TIAN, K. CHEN, The Journal of

- Chemical Physics, 150 (2019) 044907.
- [39] VELASCO C. A., GHAHNAVIYEH S. D., PISHKENARI H. N., AUTH T. and GOMPPER G., Soft Matter, 13 (2017) 5865.
- [40] ABAURREA-VELASCO C., AUTH T. and GOMPPER G., New Journal of Physics, 21 (2019) 123024.
- [41] A. Deblais, T. Barois, T. Guerin, P. H. Delville, R. Vaudaine, J. S. Lintuvuori, J. F. Boudet, J. C. Baret, H. Kellay, *Physical Review Letters*, **120** (2018) 188002.
- [42] O. FEINERMAN, I. PINKOVIEZKY, A. GELBLUM, E. FO-NIO, N. S. GOV, Nature Physics, 14 (2018) 683.
- [43] S. Reuveni, Physical Review Letters, 116 (2016) 170601.
- [44] R. E. ISELE-HOLDER, J. ELGETI, G. GOMPPER, Soft Matter, 11 (2015) 7181.
- [45] R. E. Isele-Holder, J. Jäger, G. Saggiorato, J. Elgeti, G. Gompper, *Soft Matter*, **12** (2016) 8495.
- [46] J. D. WEEKS, D. CHANDLER, H. C. ANDERSEN, The Journal of Chemical Physics, 54 (1971) 5237.
- [47] H. C. Andersen, J. D. Weeks, D. Chandler, *Physical Review A*, 4 (1971) 1597.
- [48] Redner G. S., Hagan M. F. and Baskaran A., *Physical Review Letters*, **110** (2013) .
- [49] Y. FILY, A. BASKARAN, M. F. HAGAN, Soft Matter, 10 (2014) 5609.
- [50] J. Tian, Y. Liu, J. Chen, B. Guo, S. Prasad, International Journal of Mechanical Sciences, 206 (2021) 106621.
- [51] J. ELGETI, G. GOMPPER, EPL (Europhysics Letters), 109 (2015) 58003.
- [52] S. A. MALLORY, C. VALERIANI, A. CACCIUTO, Phys. Rev. E, 90 (2014) 032309.
- [53] N. NIKOLA, A. P. SOLON, Y. KAFRI, M. KARDAR, J. TAILLEUR, R. VOITURIEZ, *Physical Review Letters*, 117 (2016) 098001.
- [54] H. R. VUTUKURI, M. HOORE, C. ABAURREA-VELASCO, L. VAN BUREN, A. DUTTO, T. AUTH, D. A. FEDOSOV, G. GOMPPER, J. VERMANT, Sculpting vesicles with active particles: Less is more (2019).
- [55] M. RAJABI, H. BAZA, T. TURIV, O. D. LAVRENTOVICH, Nature Physics, 17 (2020) 260.
- [56] H. D. Vuijk, H. Merlitz, M. Lang, A. Sharma, J. Sommer, *Physical Review Letters*, 126 (2021).
- [57] N. RAZIN, R. VOITURIEZ, J. ELGETI, N. S. GOV, Physical Review E, 96 (2017).
- [58] M. BÄR, R. GROSSMANN, S. HEIDENREICH, F. PERUANI, Annual Review of Condensed Matter Physics, 11 (2020) 441.
- [59] W. HELFRICH, Zeitschrift für Naturforschung C, 28 (1973) 693.
- [60] M. DESERNO, Chemistry and Physics of Lipids, 185 (2015) 11.
- [61] A. Šarić, A. Cacciuto, Soft Matter, 9 (2013) 6677.
- [62] F. Peruani, T. Klauss, A. Deutsch, A. Voss-Boehme, *Physical Review Letters*, **106** (2011) 128101.
- [63] S. WEITZ, A. DEUTSCH, F. PERUANI, Physical Review E, 92 (2015) 012322.
- [64] M. N. VAN DER LINDEN, L. C. ALEXANDER, D. G. A. L. AARTS, O. DAUCHOT, Physical Review Letters, 123 (2019) 098001.

Supporting Information for: Design principles for transporting vesicles with enclosed active particles

Sarvesh Uplap, ¹ Michael F. Hagan, ^{1,*} and Aparna Baskaran ^{1,†}

¹ Martin Fisher School of Physics, Brandeis University,
415 South Street, Waltham, Massachusetts 02453, USA

(Dated: September 18, 2023)

I. DETAILS OF THEORETICAL MODEL

A. Calculation of cap energy

Consider $n_{\rm r}$ rods forming smectic clusters or caps along the boundary of a circular vesicle of radius R (as shown in Fig. 3). We align a given cap along the y-axis with \hat{y} passing through the center of the cap. We can then write the height function $h(\phi) = R\cos(\phi)$ in terms of the angle ϕ (angle with respect to the y-axis). The local change in the vertical height $\Delta h(\phi)$ is then given by $\Delta h(\phi) = \sigma dh(\phi)/dx(\phi) = -\sigma \tan(\phi)$, where σ is the width of one rod. Since we are in the strong confinement limit, essentially all rods are on the vesicle surface. Assuming that all caps have approximately the optimal number of rods (which we will solve for shortly), the total number of caps is given by

$$n_{\text{cluster}} = N_{\text{rods}}/n_{\text{r}}.$$
 (1)

We now write an effective 'free energy' of the caps, U_{cluster} , that accounts for activity as well as thermal interactions among the rods and vesicle beads, given by

$$U_{\text{cluster}} = U_{\text{active}} + U_{\text{shear}} + U_{\text{interfacial}}.$$
 (2)

The first term in Eq. (2), U_{active} , is the effective rod-rod attraction arising from the rod self-propulsion and the curvature of the vesicle boundary. We assume that the strength of this attraction is proportional to the active force, $C_{\text{a}}f_{\text{a}}$ with C_{a} a proportionality constant, and thus the free energy for an undeformed (flat) cap takes the form:

$$U_{\text{active}} = -C_{\text{a}}\sigma f_{\text{a}}n_{\text{r}} = -2C_{\text{a}}f_{\text{a}}R_{\text{C}}\theta \tag{3}$$

with $R_{\rm C}$ the radius of curvature in the vicinity of the cap and $\theta = \sigma n_{\rm r}/2R_{\rm C}$ the angular extent of the cap.

The second term, $U_{\rm shear}$, accounts for the fact that curvature of the cap forces the rods to shear with respect to each other, thus reducing the extent of overlap between neighboring rods and decreasing the effective rod-rod attractions. This results in a force (linear in displacement of the rods) that resists this shear, with a shear modulus $k_{\rm shear}$. The total shear energy $U_{\rm shear}$ thus can be

$$U_{\text{shear}} = k_{\text{shear}} \int_{-\theta}^{\theta} \Delta h(\phi) R_{\text{C}} d\phi$$
$$= -2k_{\text{shear}} R_{\text{C}} \log[\cos(\theta)] \tag{4}$$

where $\theta = \sigma n_{\rm r}/2R$ is the angular extent of the cap. Note that, from the form of $U_{\rm active}, \, k_{\rm shear} \propto f_{\rm a}$.

The third term $U_{\text{interfacial}}$ is the effective interfacial energy, which accounts for the fact that rods at each edge of a cap have no neighbor in one direction and is given by

$$U_{\text{interfacial}} = -2\gamma \tag{5}$$

where $\gamma \propto f_{\rm a} \ell$ is the effective interfacial tension.

Finally, the number of caps is given by

$$n_{\text{cluster}}(\theta) = \frac{N_{\text{rods}}\sigma}{2R_{\text{C}}\theta} \tag{6}$$

so the total effective free energy of the rods can be written as

$$U_{\rm rod}(\theta) = \frac{N_{\rm rods}\sigma}{R_{\rm C}\theta} \left(\gamma + C_{\rm a}f_{\rm a}R_{\rm C}\theta - R_{\rm C}k_{\rm shear}\left[\log(\cos\theta)\right]\right)$$
(7)

B. Rigid vesicle

For the case of a rigid vesicle, we set $R_{\rm C} = R_{\rm ves}$ everywhere, and determine the optimal number and size of caps by minimizing the free energy with respect to θ :

$$\frac{\partial U_{\rm rod}}{\partial \theta} = 0 = \frac{2N_{\rm rods}\sigma}{\theta_*^2} \left[-\frac{\gamma}{R_{\rm ves}} + k_{\rm shear} \left(\log \cos \theta_* + \theta_* \tan \theta_* \right) \right]. \tag{8}$$

Defining $y(\theta) \equiv \log \cos \theta + \theta \tan \theta$, the optimal cap size is given by

$$y(\theta_*) = \frac{\gamma}{k_{\text{shear}} R_{\text{ves}}}.$$
 (9)

Plugging in the expressions for γ and k_{shear} above yields

$$y(\theta_*) = \frac{\ell \sigma}{R_{\text{ves}}}. (10)$$

calculated by integrating the local change in the vertical height of the layer along the vesicle boundary:

^{*} hagan@brandeis.edu

[†] aparna@brandeis.edu

Small angle approximation

In the limit $\theta_* \to 0$, we can expand $-\log \cos \theta \approx \theta^2/2$, giving

$$U_{\rm rod}(\theta) \approx \frac{N_{\rm rods}\sigma}{R_{\rm ves}\theta} \left(2\gamma + \frac{k_{\rm shear}}{2} R_{\rm C} \theta^2 \right)$$
$$= N_{\rm rods}\sigma \left(\frac{2\gamma}{R_{\rm ves}\theta} + k_{\rm shear}\theta \right). \tag{11}$$

Then minimization gives

$$\theta_* \cong \left(\frac{2\sigma}{R_{\text{ves}}k_{\text{shear}}}\right)^{1/2}$$

$$= \left(\frac{\ell\sigma}{R_{\text{ves}}}\right)^{1/2}, \tag{12}$$

so the number of caps goes as

$$n_{\text{cluster}} \cong N_{\text{rods}} \left(\frac{\sigma}{\ell R_{\text{ves}}}\right)^{1/2}.$$
 (13)

C. Flexible vesicle

To this point we have assumed an undeformed vesicle of radius of R. However, the propulsion force from rods within a cap locally deform the vesicle, resulting in a different local radius $R_{\rm C}$. In this section we estimate the steady-state value of $R_{\rm C}$ using a simple argument based on balancing the active force of the polar cap against the passive force from the deformed membrane. We buttress this argument with a more detailed analysis of the membrane energetics in section I E.

The membrane bending energy is given by

$$U_{\rm bend} = -\frac{\kappa_{\rm B}}{2} \int \frac{1}{R_{\rm C}^2} dS. \tag{14}$$

For simplicity, we assume that $R_{\rm C}$ is constant throughout the cap. Considering a configuration with one or two caps (e.g. the left or middle panels of Fig. 3(c) main text), the arc length in the vicinity of a cap over which the bending deformation extends corresponds to half of a circle, $\int dS = \pi R_{\rm C}$, resulting in a total bending energy for the cap of

$$U_{\rm bend} = -\frac{\pi \kappa_{\rm B}}{2R_{\rm C}} \tag{15}$$

This results in a restoring force:

$$-\frac{\partial U_{\text{bend}}(r)}{\partial r}|_{r=R_{\text{C}}} = \frac{\pi \kappa_{\text{B}}}{2R_{\text{C}}^2}$$
 (16)

This restoring force is balanced by the deforming force of the rods forming a cap along the boundary. The total active force is $n_{\rm r}f_{\rm a}$. Neglecting the variation of this force along the extent of the cap due to misalignment of

rod alignment and the vesicle normal, we can solve the force balance for the local radius in terms of the bending modulus, active force, and number of rods in the cap as

$$R_{\rm C} \cong \sqrt{\kappa_{\rm B}/f_{\rm a}n_{\rm r}}.$$
 (17)

Combining Eqs. (12), (13), and (17), we arrive at approximate expressions for the optimal cap size and number of caps for a flexible vesicle:

$$\theta_* \sim \frac{\ell^{1/2} N_{\text{rods}}^{1/4} f_{\text{a}}^{1/4}}{\kappa_{\text{B}}^{1/4}}$$
 (18)

and

$$n_{\text{cluster}}^* \sim \frac{N_{\text{rods}}^{5/4} f_{\text{a}}^{1/4}}{\ell^{1/2} \kappa_{\text{B}}^{1/4}}$$
 (19)

Finally, noting that the maximal vesicle motility occurs for the case in which there is a single cap, we estimate the scaling of the optimal value of the bending modulus $\kappa_{\rm B}^*$ in terms of the other control parameters by solving for the point at which the number of caps transitions from one to two, $n_{\rm cluster}^*(\kappa_{\rm B}^*)=2$:

$$\kappa_{\rm B}^*/f_{\rm a} \sim N_{\rm rods}^5/\ell^2.$$
(20)

This expression is compared to simulation results in Fig. 5(a) of the main text.

D. Maximum number of rods for the high vesicle motility state

From section III of the main text, we know that membrane deformation is essential to stabilize polar-aligned caps. Thus, there is an upper bound on the bending modulus $\kappa_{\rm B} \leq \kappa_{\rm B}^{\rm max}$ for which we can observe stable 1-cap states and the corresponding peak in vesicle motility. In this section we estimate this bending modulus value, and show that it leads to a maximum number of enclosed rods above which there will be no stable one-cap state for any parameter value, and thus no highly motile vesicle state.

To estimate $\kappa_{\rm B}^{\rm max}$, we set the curvature radius to the unperturbed vesicle radius, $R_{\rm C}=R_{\rm ves}$, in the force balance (Eq. (16)), resulting in

$$\frac{\pi \kappa_{\rm B}^{\rm max}}{2R_{\rm ves}} = n_{\rm r} f_{\rm a}.$$
 (21)

The largest active force in this state will correspond to the largest possible polar cap. To that end, note that there is a maximum cap size, since once $\sigma \tan \theta > \ell$ the cap must break: $\theta_{\rm max} = \tan^{-1} \ell \approx \frac{\pi}{2} - 1/\ell$. Thus, for large aspect-ratio rods, the largest polar cap that can form will fill a semicircle on the vesicle surface with $\theta_{\rm max} \approx \pi/2$. Further, for $\kappa_{\rm B} \geq \kappa_{\rm B}^{\rm max}$ the curvature radius within this cap will be equal to the unperturbed vesicle

radius, from which we obtain that the number of rods in the maximal cap will be $n_{\rm r}^{\rm max} = \pi R_{\rm ves}/\sigma$. Substituting this into Eq. (21), and setting the cap size to the total number of enclosed rods, $n_{\rm r} = N_{\rm rods}$ results in

$$\kappa_{\rm B}^{\rm max} \cong N_{\rm rods} f_{\rm a} R_{\rm ves}^2 / \sigma^2.$$
(22)

Since Eqs. (20) and (22) respectively set lower and upper bounds on the bending modulus for the stable 1-cap state, we expect to no longer observe this state when these two bounds merge. Solving for this point in terms of the number of enclosed rods results in

$$N_{\text{rods}}^{\text{max}} \cong (\ell R_{\text{ves}}/\sigma)^{2/5}$$
. (23)

For $N_{\rm rods} \gtrsim N_{\rm rods}^{\rm max}$ we expect the system to transition directly from states containing two or more caps to trans sient cap states. For the vesicle size that we focus on in this work, $R_{\text{ves}} = 80\sigma$, Eq. (23) gives a maximum rod number of order 10 (to within a scaling constant), which is consistent with the observation that we do not observe stable 1-cap states for $N_{\rm rods} \gtrsim 60$.

$\mathbf{E}.$ Detailed analysis of membrane energy

We now consider a more complete analysis of the effective free energy of the membrane and rod configurations. We will arrive at the same expressions as obtained in section IC.

For simplicity, we assume a geometry in which the curvature is the same at each cap, and the vesicle is flat between caps; i.e., it forms a regular polygon with rounded vertices, with the number of vertices equal to the number of caps. We denote the length of each flat region as l, and note that the total angle swept out by the curved regions must be $n_{\text{cluster}}\theta_* = 2\pi$, and so the total arc length of cap regions is $2\pi R_{\rm C}$. Assuming a fixed vesicle perimeter $2\pi R_{\rm ves}$, we can then obtain the length of the flat regions

$$l = \frac{1}{n_{\text{cluster}}} 2\pi (R_{\text{ves}} - R_{\text{C}}). \tag{24}$$

Notice that our geometry requires $R_{\rm C} \leq R_{\rm ves}$.

In this geometry, we can write the vesicle energy as a function of two terms

$$U_{\text{ves}} = U_{\text{bend}} + U_{\text{f}} \tag{25}$$

with the bending energy given by the usual Helfrich form

$$U_{\text{bend}} = \frac{\kappa_{\text{B}}}{2} 2\pi R_{\text{C}} \left(\frac{1}{R_{\text{C}}}\right)^{2}$$
$$= \frac{\pi \kappa_{\text{B}}}{R_{\text{C}}}$$
(26)

with $\kappa_{\rm B}$ the bending modulus.

The energy due to the rod force is easiest to consider in the case of 2 caps, for which half of the rods are on either

side of the vesicle, stretching it along the \hat{x} axis with a total force $f = f_a N_{\text{rods}}/2$. The energy contribution is then

$$U_{\rm f}(n_{\rm cluster} = 2) = -fl$$

= $-\pi f_{\rm a} N_{\rm rods}(R_{\rm ves} - R_{\rm C}).$ (27)

For $n_{\text{cluster}} > 2$, in our geometry, the force on each domain will approximately be given by f $N_{\rm rods}f_{\rm a}/n_{\rm cluster}$, and will be directed along an axis from the center to vertex, with length $l_{\text{vert}} = \frac{l}{2\sin(\pi/n_{\text{cluster}})}$ (from the formula for the inscribed circle of a polygon), giving

$$U_{\rm f} = -f_{\rm a} N_{\rm rods} \frac{n_{\rm cluster} - 1}{n_{\rm cluster}} \frac{2\pi (R_{\rm ves} - R_{\rm C})}{2n_{\rm cluster} \sin(\pi/n_{\rm cluster})}. (28)$$

However, in the limit of large $n_{\rm cluster}$, $\sin(\pi/n_{\rm cluster}) \approx$ $\pi/n_{\rm cluster}$, and the expression reduces to

$$U_{\rm f} = -f_{\rm a}N_{\rm rods}\frac{n_{\rm cluster} - 1}{n_{\rm cluster}}2\pi(R_{\rm ves} - R_{\rm C}). \tag{29}$$

To simplify the analysis, let us eliminate the dependence on $n_{\rm cluster}$ from this expression, and take the result for $n_{\text{cluster}} = 2 \text{ for all } n_{\text{cluster}} \geq 2$:

$$U_{\rm f} \approx -f_{\rm a} N_{\rm rods} \pi (R_{\rm ves} - R_{\rm C})$$
 for $n_{\rm cluster} \ge 2$. (30)

Note that the case of $n_{\text{cluster}} = 1$ is special, since here the force from the rods does not cancel and the vesicle undergoes net motion.

At steady state, the total drag on the vesicle and rods must balance the propulsive force from the rods. Assuming drag coefficients ξ and $\xi_{\rm V}$ for rods and vesicle beads respectively, and the number of vesicle beads as N_{ves} , the steady-state velocity will then be given by

$$v = \frac{N_{\text{rods}} f_{\text{a}}}{N_{\text{rods}} \xi + N_{\text{ves}} \xi_{\text{V}}}$$
(31)

The net force stretching the vesicle is then given by roughly

$$f \approx v N_{\text{ves}} \xi_{\text{V}}$$

$$= N_{\text{rods}} f_{\text{a}} \frac{N_{\text{ves}} \xi_{\text{V}}}{N_{\text{ves}} \xi_{\text{V}} + N_{\text{rods}} \xi}$$
(32)

$$\approx N_{\text{ves}} f_{\text{a}} \frac{\xi_{\text{V}}}{\xi} \quad \text{for } N_{\text{ves}} \xi_{\text{V}} \ll N_{\text{rods}} \xi \qquad (33)$$

$$\approx N_{\text{rods}} f_{\text{a}} \quad \text{for } N_{\text{ves}} \xi_{\text{V}} \gg N_{\text{rods}} \xi. \qquad (34)$$

$$\approx N_{\text{rods}} f_{\text{a}}$$
 for $N_{\text{ves}} \xi_{\text{V}} \gg N_{\text{rods}} \xi$. (34)

The situation is particularly nice in the last limit, vesicle drag dominated $N_{\rm ves}\xi_{\rm V}\gg N_{\rm rods}\xi$, because in that case we can use Eq. (30) for all numbers of caps:

$$U_{\rm f} \approx -f_{\rm a} N_{\rm rods} \pi (R_{\rm ves} - r) \qquad \forall n_{\rm cluster}.$$
 (35)

Importantly, we find that this limit approximately applies in our simulations for most parameters that we consider.

Determine optimal curvature and cap size

We now consider the full energy in the large vesicle drag limit, setting $\sigma = 1$ (all lengths in units of σ):

$$\frac{U}{N_{\rm rods}f_{\rm a}\sigma} = \frac{\pi\bar{\kappa}}{N_{\rm rods}R_{\rm C}} - \pi(R_{\rm ves} - r) + \frac{2\bar{\gamma}}{R_{\rm C}\theta} - 2\bar{k}\frac{1}{\theta}\log\cos\theta$$
(36)

with $\bar{\kappa} \equiv \kappa_{\rm B}/f_{\rm a}\sigma^2$, $\bar{\gamma} \equiv \gamma/f_{\rm a}\sigma$, and $\bar{k} \equiv k_{\rm shear}/f_{\rm a}$. Differentiating with respect to θ gives

$$\log \cos \theta_* + \theta \tan \theta_* = \frac{\bar{\gamma}}{\bar{k} R_{\rm C}^*}$$
 (37)

Differentiating with respect to $R_{\rm C}$ gives

$$0 = -\left(\frac{\pi\bar{\kappa}}{N_{\text{rods}}} + \frac{2\bar{\gamma}}{\theta}\right) \frac{1}{r^2} + \pi \tag{38}$$

SO

$$R_{\rm C}^* = -\left(\frac{\bar{\kappa}}{N_{\rm rods}} + \frac{2\bar{\gamma}}{\pi\theta_*}\right)^{1/2}.$$
 (39)

We must solve Eqs. 37 and 39 numerically.

F. Small angle approximation to determine the optimal curvature and cap size

We now consider the full energy in the small angle approximation and large vesicle drag limit

$$\frac{U}{N_{\rm rods}f_{\rm a}\sigma} = \frac{\pi\bar{\kappa}}{N_{\rm rods}R_{\rm C}} - \pi(R_{\rm ves} - R_{\rm C}) + \frac{2\bar{\gamma}}{R_{\rm C}\theta} + \bar{k}\theta$$
(40)

Differentiating with respect to θ gives

$$0 = -\frac{2\bar{\gamma}}{R_C \theta^2} + \bar{k} \tag{41}$$

so

$$\theta_* = \left(\frac{2\bar{\gamma}}{R_{\rm C}^* \bar{k}}\right)^{1/2} \tag{42}$$

If we plug in the expected dependence of $\gamma \propto f_{\rm a} \ell$ and $k_{\rm shear} \propto f_{\rm a}$, we obtain

$$\theta_* \cong \left(\frac{\ell}{R_{\rm C}}\right)^{1/2} \tag{43}$$

as above.

Differentiating with respect to $R_{\rm C}$ gives

$$0 = -\left(\frac{\pi\bar{\kappa}}{N_{\text{rods}}} + \frac{2\bar{\gamma}}{\theta}\right) \frac{1}{R_C^2} + \pi \tag{44}$$

so

$$R_{\rm C}^* = -\left(\frac{\bar{\kappa}}{N_{\rm rods}} + \frac{2\bar{\gamma}}{\pi\theta_*}\right)^{1/2}.$$
 (45)

Plugging in Eq. (42) gives

$$R_{\rm C}^* = -\left[\frac{\bar{\kappa}}{N_{\rm rods}} + \left(\frac{2}{\pi^2}\bar{\gamma}\bar{k}R_{\rm C}^*\right)^{1/2}\right]^{1/2}.$$
 (46)

If we plug in the expected dependence of γ and k_{shear} , we obtain

$$R_{\rm C}^* = \left[\frac{\bar{\kappa}}{N_{\rm rods}} + \left(\frac{R_{\rm C}^*}{\ell} \right)^{1/2} \right]^{1/2}. \tag{47}$$

This gives us two limits. Noting that $R_{\rm C} \leq R_{\rm ves}$

$$R_{\rm C}^* \approx \left(\frac{\bar{\kappa}}{N_{\rm rods}}\right)^{1/2}$$
 for $\bar{\kappa} \gg N_{\rm rods} \left(\frac{R_{\rm ves}}{\ell}\right)^{1/2}$ (48)

$$R_{\rm C}^* \approx \ell^{-1/3}$$
 for $\bar{\kappa} \ll N_{\rm rods} \left(\frac{R_{\rm ves}}{\ell}\right)^{1/2}$. (49)

The latter limit is not physical, as we should not have $R_{\rm C} < 1$ (measured in units of σ). This is because our small angle approximation breaks down once $R_{\rm C}^* \sim \ell$, and we must return to the full expression with $-\log \cos \theta$.

In the limit of large $\bar{\kappa}$, note that the requirement $R_{\rm C} \leq R_{\rm ves}$ gives a 'critical' $\bar{\kappa}$ above which there is essentially no bending of the vesicle:

$$\bar{\kappa}_{\rm c} = N_{\rm rods} \left[R_{\rm ves}^2 - \frac{\sqrt{2}}{\pi} \left(\frac{R_{\rm ves}}{\ell} \right)^{1/2} \right]$$

$$\bar{\kappa}_{\rm c} \approx N_{\rm rods} R_{\rm ves}^2. \tag{50}$$

Finally, in the limit of large $\bar{\kappa}$, we obtain

$$\theta_* \sim \frac{\ell^{1/2} N_{\mathrm{rods}}^{1/4}}{\bar{\kappa}^{1/4}} \quad \text{for } \bar{\kappa} \gg N_{\mathrm{rods}} \left(\frac{R_{\mathrm{ves}}}{\ell}\right)^{1/2} \quad (51)$$

and

$$n_{\rm cluster}^* \sim \frac{N_{\rm rods}^{5/4}}{\ell^{1/2}\bar{\kappa}^{1/4}} \quad \text{for } \bar{\kappa} \gg N_{\rm rods} \left(\frac{R_{\rm ves}}{\ell}\right)^{1/2}$$
 (52)

Finally, noting that the maximal vesicle motility occurs for the case in which there is a single cap, we estimate the scaling of the optimal value of the bending modulus $\kappa_{\rm B}^*$ in terms of the other control parameters by solving for the point at which the number of caps transitions from one to two, $n_{\rm cluster}^*(\kappa_{\rm B}^*) = 2$. Using $\bar{\kappa} \equiv \kappa_{\rm B}/f_{\rm a}\sigma^2$ and Eq. (52), we obtain

$$\kappa_{\rm B}^*/f_{\rm a} \sim N_{\rm rods}^5/\ell^2.$$
 (53)

Notice that Eqs. (52) and (53) match the results of section I C.

II. DETAILS OF ANALYSIS OF SIMULATION DATA

A. Simulation details

The equations of motion are integrated forward in time using HOOMD (version 2.9.6)[1, 2]. We use the Brownian integrator for the rods and the Langevin integrator for the vesicle. In HOOMD, all units are derived from base units of energy, length, and mass. In our simulations, we set these as $k_{\rm B}T$, the rod diameter σ , and the bead mass m. This gives rise to a time unit of $t_{\rm sim} = \sqrt{m\sigma^2/k_{\rm B}T}$. For presentation clarity in the main text, we present results in terms of the more natural time unit of $\tau_{\rm s}$, the time for a bead with the diameter of a rod to diffuse its diameter. These are related as $\tau_{\rm s} = \sqrt{\frac{\sigma^2 \xi_0^2}{mk_{\rm B}T}} t_{\rm sim}$, and in the simulations, we set the bead mass m=1 and $\xi_0=1\,m/t_{\rm sim}$.

We set the time step for both integrators to $\delta t = 0.0001 t_{\rm sim}$.

To characterize the rod self-propulsion, we note that the active velocity of an isolated rod is given by $v_{\rm a}=f_{\rm a}/\xi^{\rm T}$, which for our parameters is $v_{\rm a}=0.1f_{\rm a}/\xi_0=0.1f_{\rm a}\sigma^2/k_{\rm B}T\tau_{\rm s}$. For an isolated rod, we can also define a Peclet number as Pe $\equiv v_{\rm a}/\sigma D_{\rm r}=v_{\rm a}\xi^{\rm R}/\sigma\xi^{\rm T}=100f_{\rm a}\sigma/k_{\rm B}T$, where $v_{\rm a}=f_{\rm a}/\xi$ is the active velocity of a rod and $D_{\rm r}=k_{\rm B}T/\xi^{\rm R}$ is the rotational diffusion constant. However, due to the complex interplay between rod self-propulsion forces and passive elastic vesicle forces, there is not a well-defined Peclet number that characterizes the balance between active and diffusive behaviors in the vesicle system.

We initialize the system by placing the vesicle beads equally spaced along a circle at their equilibrium radius $R_{\rm ves}=80\sigma$, and then placing the rods randomly inside the vesicle, excluding overlaps. We then thermalize the system in the absence of the active force, by setting $f_{\rm a}=0$ and linearly ramping the temperature from 0 at t=0 to $k_{\rm B}T$ at $t=100\,t_{\rm sim}$, and setting $\epsilon=0$ such that $U_{\rm WCA}=0$. During the thermalization we set the the non-bonded interactions between all pairs of vesicle-rod and rod-rod beads to a Yukawa potential:

$$U_{\rm Y} = \epsilon_{\rm Y} \frac{e^{-k_{\rm Y}} r}{r} \tag{54}$$

where r is the inter-bead separation, $\epsilon_{\rm Y}=5\,k_{\rm B}T$, and $k_{\rm Y}=2.75\sigma^{-1}$. The values are chosen such that the beads are not subject to large forces on being placed inside the vesicle. After these initialization and thermalization steps, we turn on the active force, set $k_{\rm B}T=1$, $\epsilon=k_{\rm B}T$ and $\epsilon_{\rm Y}=0$. Except for one parameter set, each simulation is performed for $20000t_{\rm sim}$ after initialisation, with particle positions and velocities recorded every $10t_{\rm sim}$. For the parameter set $N_{\rm rods}=30$, $f_{\rm a}=3$, $\ell/\sigma=6$, we performed simulations until $40000t_{\rm sim}$ to confirm that observables were not changed by simulating to longer times. Based on the total deformation energy of the vesicle, we

find that the system reaches steady state by $t = 5000t_{\rm sim}$ at all parameter values (see Fig. 1), and thus we evaluate statistics based on results from $t > 5000t_{\rm sim}$.

B. Determining steady states

To determine if the system reached steady state, we examined the total deformation energy of the vesicle $E_{\rm total}$ as a function of simulation time. The deformation energy is given by:

$$E_{\text{total}} = \sum_{i=1}^{N_{\text{ves}}-1} U_{\text{stretch}}(r_{i,i+1}) + \sum_{i=2}^{N_{\text{ves}}-1} U_{\text{bend}}(\phi_{i-1,i,i+1})$$
(55)

Fig. 1 shows the total deformation energy (relative to the steady-state value) for vesicles with bending modulus values ranging from floppy to stiff, and two values of $N_{\rm rods}$. We see that the vesicle deformation energy increases rapidly after the initialization and thermalization phases of the simulation (for time $> 100t_{\rm sim}$), as the rods moved to the vesicle boundary and deform the vesicle. For the lowest active force that we consider in this work, $f_{\rm a}=3k_{\rm B}T$, it takes about $t\approx 5000t_{\rm sim}$ for the caps to organize into a steady state, as evidenced by the saturation of the total deformation energy to fluctuations about a mean value. Steady states are reached more quickly for larger values of the active force. Notice that, for low values of $\kappa_{\rm B}$, the deformation energy remains roughly constant with small fluctuations about the mean once the rods form stable caps. Counterintuitively though, large values of $\kappa_{\rm B}$ give rise to large fluctuations in the deformation energy because the rods form transient caps (see results section in main text).

Based on these observations, we performed measurements for all statistical quantities in this work from times $t > 5000 t_{\rm sim}$.

C. Vesicle motions are uncoupled to active forces for spherical particles

As noted in the main text, in the limit of spherical particles, the particle orientation and corresponding active force are uncoupled to the vesicle configuration because there are no particle-particle or particle-vesicle torques. Consequently, the mean net active force transferred from the particles to the vesicle should vanish, and the enclosed active particles will not affect the vesicle motion, even in the case of floppy vesicles for which the particles cluster and significantly deform the vesicle boundary. In particular, the path traced by the center of mass depends on the net active force on the vesicle: $\sum_{i=1}^{N_{\rm rods}} f_{\rm a} \hat{\nu}_i.$ Since the persistence length of the particle motions $f_{\rm a} \xi^{\rm R}/\xi^{\rm T} = 300\sigma$ is much larger than the vesicle radius, we are in the strong confinement limit and the particles spend all their time at the vesicle boundary.

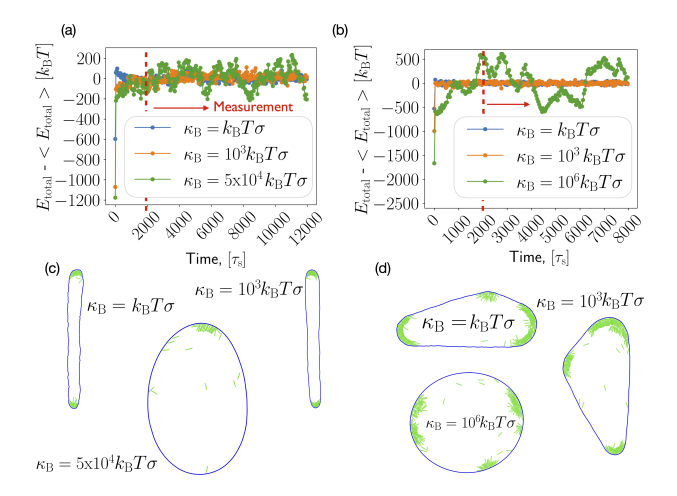


FIG. 1. The mean total deformation energy relative to its steady-state value, $E_{\rm total} - \langle E_{\rm total} \rangle$ as a function of time (starting after the initialization and thermalization steps have been completed) for indicated values of the vesicle bending modulus $\kappa_{\rm B}$ and (a) $N_{\rm rods}=30$, $f_{\rm a}=3k_{\rm B}T$, $\ell/\sigma=6$ and (b) $N_{\rm rods}=150$, $f_{\rm a}=3k_{\rm B}T$, $\ell/\sigma=6$. (c), (d) Typical steady-state configurations for vesicles with indicated values of the bending modulus and (c) $N_{\rm rods}=30$ and (d) $N_{\rm rods}=150$. Note that the caps are transient in the vesicles with a large stiffness values $\kappa_{\rm B}=5\times10^4\,k_{\rm B}T\sigma$ in (c) and $\kappa_{\rm B}=10^6\,k_{\rm B}T\sigma$ in (d)).

Therefore, since f_a is a constant, the net force on the vesicle depends only on the orientation $\hat{\nu}$ of the beads. In the absence of interparticle or particle-vesicle torques, $\hat{\nu}$ is independent of the local particle density or vesicle curvature, and thus independent of the cluster configuration.

To provide numerical evidence for the uncoupling of vesicle motions and cluster configurations for spherical particles, Fig. 2 shows the path traced by the center of mass of vesicles with different values of $\kappa_{\rm B}$ \in $\{1..10^6\}k_{\rm B}T\sigma$ and encapsulated spherical active beads of radius 1σ . To show that the vesicle trajectory is independent of the cluster configuration, we performed each of these simulations with the same initial conditions and the same random forces on the vesicle beads and the active beads, i.e $\eta_i^{\text{ves}}(t)$, $\eta_i^{\text{R}}(t)$, $\eta_i^{\text{T}}(t)$ $(i \in N_{\text{rods}}, i \in N_{\text{ves}})$, throughout the trajectories. The images below the plot show typical vesicle configurations for floppy and stiff vesicles, demonstrating that the cluster configurations depend sensitively on vesicle stiffness. Yet, we see that the path traced by the center of mass is very similar for each vesicle, independent of its stiffness.

D. Measurement of optimal stiffness

We estimated the optimal stiffness, which gives rise to the maximal vesicle motility, by fitting a polynomial of degree 4 to the measured vesicle diffusion coefficient as a function the vesicle bending modulus. We restricted the

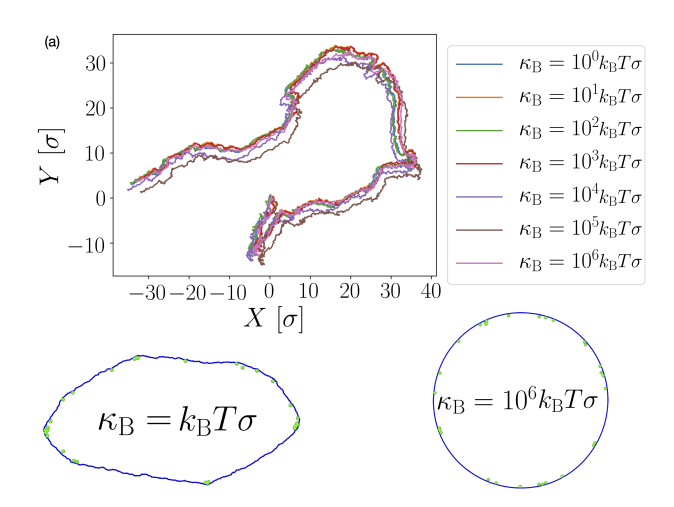


FIG. 2. The path traced by the center of mass for vesicles with indicated values of the bending modulus ($\kappa_{\rm B} \in \{1..10^6\}$) enclosing $N_{\rm rods}=30$ active spherical beads with unit radius ($\ell/\sigma=1$) and an active force of $f_{\rm a}=3k_{\rm B}T/\sigma$. All the simulations have the same random seed and thus identical sets of random forces on the active and vesicle beads. Bottom: Snapshots of typical configurations of floppy (left) and stiff (right) vesicles. Active beads are enlarged for better visualisation.

fit to data points near the maximum, and computed the optimal stiffness as the stiffness that maximizes the fit polynomial. Fig. 3 shows plots of the measured diffusion coefficients as a function of vesicle bending modulus and the corresponding polynomial fits for different values of $N_{\rm rods}$ and $f_{\rm a}$.

E. Cap recognition method

To identify caps, we take a coarse-grained view of the vesicle by placing it in a grid of size $s_{\rm gp} \times s_{\rm gp}$, with $s_{\rm gp} = 90$ the grid size. Each tile in this grid, denoted by $r_{\rm gp} \equiv \{x_{\rm gp}, y_{\rm gp}\}$ represents an area of $s_{\rm res}\sigma \times s_{\rm res}\sigma$, with $s_{\rm res} = 4$ the resolution. The vesicle center of mass is at the origin of the grid (or in the central tile), $r_{\rm gp} = \{s_{\rm gp}/2, s_{\rm gp}/2\}$. Rod beads are assigned to tiles in this grid based on their position with respect to the vesicle center of mass, $\{\delta x_{i,j}, \delta y_{i,j}\}$, where $\delta x_{i,j} = x_{i,j} - x_{\rm com}$, $\delta y_{i,j} = y_{i,j} - y_{\rm com}$ for the j^{th} bead in the i^{th} rod. $\{x_{i,j}, y_{i,j}\}$ is the position of the bead and $\{x_{\rm com}, y_{\rm com}\}$ is the position of the vesicle center of mass. The corresponding position in the grid $x_{\rm gp}, i, j = (\delta x_{i,j} + 2s_{\rm gp})/s_{\rm res}$, $y_{\rm gp}, i, j = (\delta y_{i,j} + 2s_{\rm gp})/s_{\rm res}$. Each rod bead is assigned to a tile at position $\{x_{\rm gp}, i, j, y_{\rm gp}, i, j\}$ in the grid.

A pseudo-cluster is then defined as a collection of tiles that each have at least one bead assigned to them and share at least one common edge, thus forming a connected region in the grid. The number of rods in the pseudo-cluster $N_{\rm pc}$ are counted and the angle $\Phi_{i,i'} = \cos^{-1}(\hat{\nu}_i \cdot \hat{\nu}_{i'})$ is measured for each pair of rods in the pseudo-cluster, where $\hat{\nu}_i$, $\hat{\nu}_{i'}$ are the orientation of the

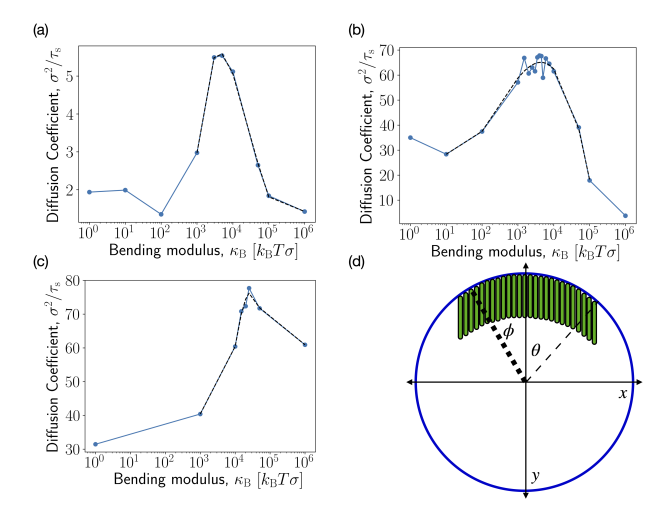


FIG. 3. The vesicle diffusion coefficient as a function of vesicle bending modulus (blue dots) for (a) $N_{\rm rods}=30$, $f_{\rm a}=3k_{\rm B}T/\sigma$, (b) $N_{\rm rods}=20$, $f_{\rm a}=6k_{\rm B}T/\sigma$, and (c) $N_{\rm rods}=30$, $f_{\rm a}=9k_{\rm B}T/\sigma$. The black dashed line shows a polynomial fit in the vicinity of the maximum, which is used to infer the optimal bending modulus. (d) Cartoon of active rods forming a cap along an undeformed vesicle of radius R, the center of which is placed at the origin. The symbol ϕ gives the angular position at arbitrary points within the cap, which extends from $-\theta < \phi \le \theta$.

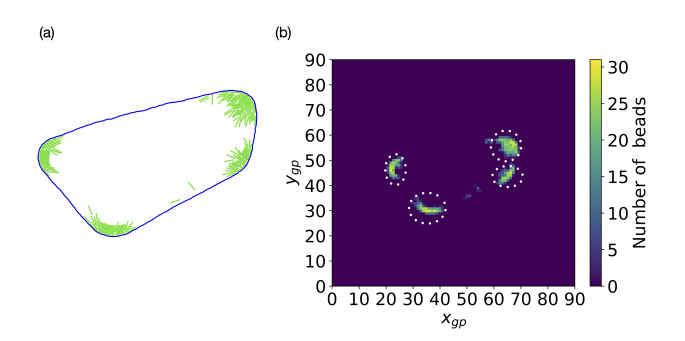


FIG. 4. (a) Snapshot of a typical configuration for a vesicle with $\kappa_{\rm B}=k_{\rm B}T\sigma$, $N_{\rm rods}=150$, and $f_{\rm a}=3k_{\rm B}T/\sigma$. The rods form four distinct caps. (b) Rod density profile averaged over the steady state for the parameters shown in (a). The heat map shows the number of rod pseudoatoms within each grid point. The cap-identification algorithm described in the text detects four caps, which are marked by white circles. The caps each have more than three rods that are aligned (parallel to each other).

 i^{th} and the i'^{th} rod in the pseudo cluster. A pseudo-cluster is identified as a cap if $N_{\rm pc} \geq 3$ and $\Phi_{i,i'} < 0.15$ for three or more pairs of rods (i.e., three or more pairs of rods are aligned). Fig. 4(a) shows a snapshot of a vesicle enclosing $N_{\rm rods} = 150$ rods organised into four caps. Fig. 4(b) shows a heat map of the grid with the color indicating the number of beads assigned to each tile. Four distinct caps can be seen that satisfy the criteria for the number of rods and the rod alignment. We measure the number of caps for each recorded simulation frame, and

we compute the mean number of caps by averaging over 100 independent trials for each parameter set.

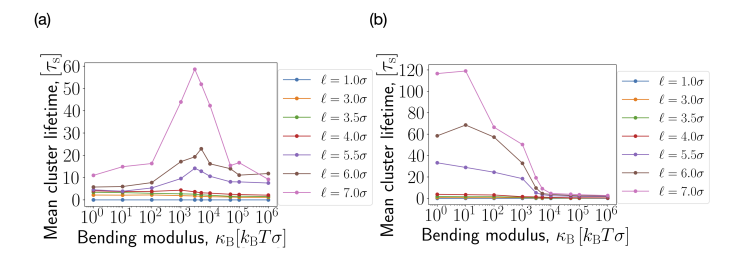


FIG. 5. Mean cap lifetimes (τ) for 1-cap (a) and 2-cap (b) configurations as a function of vesicle bending modulus for rods with varying lengths, $N_{\rm rods}=30$, and $f_{\rm a}=3k_{\rm B}T/\sigma$. The lifetime of the 1-cap configuration increases as a function of rod length ℓ , and for long rods the the lifetime is maximum at the optimal stiffness. The lifetime of the 2-cap configuration increases as a function of rod length ℓ at low stiffness values, while for long rods the lifetime decreases with increasing vesicle stiffness. This coincides with the increase in mean lifetime of the 1-cap state.

We measure cap lifetimes by counting the number of simultaneous frames during which the system has the given number of caps, and averaging over 100 independent trials for each parameter set. Fig. 5 (a) shows the lifetimes of the 1-cap and 2-cap configurations as a function of vesicle bending stiffness. The cap lifetimes increases with rod aspect ratio ℓ . The lifetime of 1-cap configurations is maximized at the optimal bending stiffness for a given parameter set $\{N_{\text{rods}}, f_{\text{a}}\}$. In Fig. 5(a) the maximum lifetime for the 1-cap state is at the optimal stiffness value $\kappa_{\rm B}^* \approx 3000 k_{\rm B} T \sigma$. For floppier vesicles $\kappa_{\rm B} < \kappa_{\rm B}^*$, the 2-cap configuration is dominant, as evidenced by the fact that lifetime of the 2-cap configuration is larger than that of the 1-cap configuration (Fig. 5 (b)). The lifetimes of 2-cap configurations gradually decrease with vesicle stiffness, as 1-cap configurations become more favorable. For stiffer-than-optimal vesicles $\kappa_{\rm B} > \kappa_{\rm B}^*$, the rods form transient caps, resulting in a reduction in the 1-cap lifetimes.

F. Characterizing the dynamics of the center of mass of the vesicle

As we saw in the main text, the mean square displacement of the vesicle center of mass is well described by a persistent random walk. Hence, it is suggestive to map the motion of the vesicle to the well studied active Brownian particle model. When we attempt to do this, we find that the self propulsion velocity v_0 is enhanced at the optimal stiffness value, while the rotational diffusion coefficient $D_{\rm r}$ does not exhibit any systematic dependence on the underlying model parameters (see Fig. 6).

The persistent random walk of the vesicle emerges from the complex dynamics of the self organized rod clusters and the deformations of the vesicle itself. Hence, it is useful to characterize the center-of-mass dynamics in terms of more fundamental quantities driving the motion, $\bar{F}_{\rm net} = \sum_{i=1}^{N_{\rm rods}} f_{\rm a} \hat{\nu}_i$, the net force exerted by the active rods on the vesicle and $\bar{v}_{\rm com} = N_{\rm ves}^{-1} \sum_{j=1}^{N_{\rm ves}} \bar{v}_j$, the center-of-mass velocity. The rotational diffusion coefficient, or equivalently the persistence time of the random walk, emerges from the dynamics of $\bar{F}_{\rm net}$ and $\bar{v}_{\rm com}$. The simplest postulate for this would be to consider the vesicle motion as described by a Langevin equation of the form

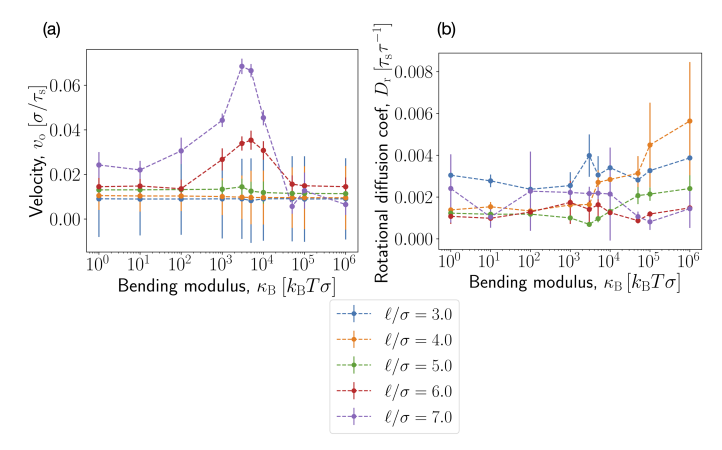


FIG. 6. Self-propulsion velocity v_0 (a) and rotational diffusion coefficient $D_{\rm r}$ (b) of the vesicle center of mass when its dynamics is modelled as an active Brownian particle (ABP). Results are shown for vesicle radius $R_{\rm ves}=80\sigma$ and activity $f_{\rm a}=3k_{\rm B}T$, for various rod lengths and vesicle stiffness values. The velocity is measured by fitting a quadratic functino to the MSD equation in the ballistic limit (fitting is performed on points where the slope of MSD is greater than 1.8). The velocity of the vesicle center of mass is independent of vesicle stiffness for short rods, but the velocity is enhanced at the optimal stiffness for long rods. The rotational diffusion coefficient is extracted from the full fit for the mean square displacement of an ABP.

$$M_{\rm V} \frac{d\bar{v}_{\rm com}(t)}{dt} = -N_{\rm ves} \xi_{\rm V} \bar{v}_{\rm com}(t) + \bar{F}_{\rm net}(t)$$
 (56)

where $M_{\rm V}=N_{\rm ves}\cdot 1$ is the total mass of the vesicle, and $\xi_{\rm V}$ is the translational drag coefficient on the vesicle beads. Solving for $\bar{v}_{\rm com}$, we have

$$\bar{v}_{\rm com}(t) = \bar{v}_{\rm init}e^{-t/\lambda_{\rm ves}} + \frac{e^{-t/\lambda_{\rm ves}}}{M_{\rm V}} \int_0^t e^{s/\lambda_{\rm ves}} \bar{F}_{\rm net}(s) ds.$$
(57)

where we use the notation $\lambda_{\rm ves} = M_{\rm V}/N_{\rm ves}\xi_{\rm V}$ for compactness. Thus, the the velocity auto-correlation function $\langle \bar{v}_{\rm com}(t_1) \cdot \bar{v}_{\rm com}(t_2) \rangle$ is of the form

$$\begin{split} &\langle \bar{v}_{\rm com}(t_1) \cdot \bar{v}_{\rm com}(t_2) \rangle = \\ & \left\langle \left[\bar{v}_{\rm init} e^{-t_1/\lambda_{\rm ves}} + \frac{e^{-t_1/\lambda_{\rm ves}}}{M_{\rm V}} \int_0^{t_1} e^{s/\lambda_{\rm ves}} \bar{F}_{\rm net}(s) ds \right] \\ & \cdot \left[\bar{v}_{\rm init} e^{-t_2/\lambda_{\rm ves}} + \frac{e^{-t_2/\lambda_{\rm ves}}}{M_{\rm V}} \int_0^{t_2} e^{w/\lambda_{\rm ves}} \bar{F}_{\rm net}(w) dw \right] \right\rangle. \end{split}$$

When averaged over all possible initial velocities, the cross terms vanish and we get

$$\langle \bar{v}_{\text{com}}(t_1) \cdot \bar{v}_{\text{com}}(t_2) \rangle = \langle |\bar{v}_{\text{init}}|^2 \rangle e^{-(t_1 + t_2)/\lambda_{\text{ves}}}$$

$$\frac{e^{-(t_2 + t_1)/\lambda_{\text{ves}}}}{M_{\text{V}}^2} \int_0^{t_1} \int_0^{t_2} e^{(w+s)/\lambda_{\text{ves}}} \langle \bar{F}_{\text{net}}(s) \cdot \bar{F}_{\text{net}}(w) \rangle \, ds \, dw.$$
(58)

As shown in the main text, the force correlations are exponential, i.e., of the form $\langle \bar{F}_{\rm net}(s) \cdot \bar{F}_{\rm net}(w) \rangle = A^2 e^{-|s-w|/\lambda_{\rm f}}$ with A a constant. Thus, the velocity autocorrelation function in the long time limit, $\lim_{t_1 \to \infty}$, $\lim_{t_2 \to \infty}$, is of the form

$$\frac{\langle \bar{v}_{\text{com}}(t_1) \cdot \bar{v}_{\text{com}}(t_2) \rangle}{M_{\text{V}}^2} \left[\frac{\lambda_{\text{f}}^2 e^{-(t_1 - t_2)/\lambda_{\text{f}}} - \lambda_{\text{f}} \lambda_{\text{ves}} e^{-(t_1 - t_2)/\lambda_{\text{ves}}}}{\lambda_{\text{f}}^2 - \lambda_{\text{ves}}^2} \right].$$
(59)

To test the validity of this simple model for the center-of-mass dynamics of the vesicle, we compare the measured velocity auto-correlation function with this expression in Fig. 7. We find that this expression does not fit the data consistently across all parameters. These discrepancies reflect the fact that the dynamics of the vesicle is more complex than this simple Langevin Model, due to timescales associated with reorganization of the enclosed rods. In particular, note that when $\lambda_f \gg \lambda_{\rm ves}$, $\lambda_{\rm v} = \lambda_{\rm f}$. This behavior is consistent with the simulation data for long rods, where the clusters persist for long times, but short rods have distinct time scales associated with the fluctuations of velocity and force (Fig. 8).

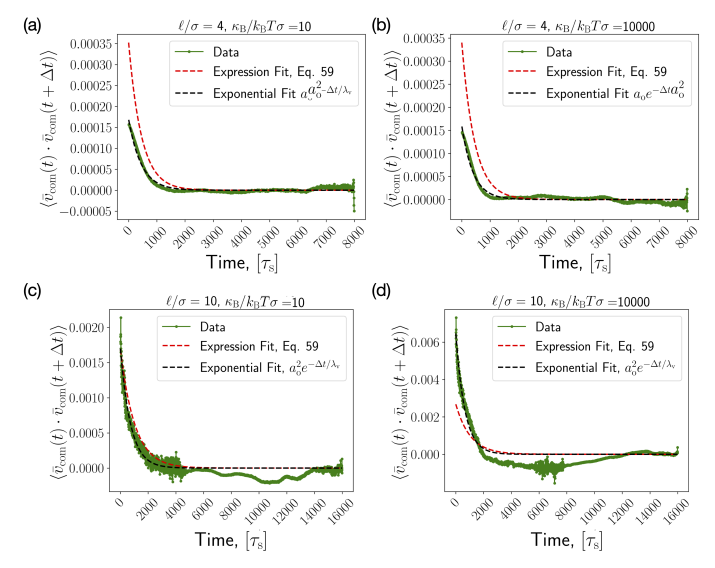


FIG. 7. Comparison of the predictions of the simple Langevin model for the vesicle center of mass for $\bar{v}_{\rm com}$ to the simulation results, for an illustrative set of parameter values. We use A and $\lambda_{\rm f}$ obtained from the data and $\lambda_{\rm ves}$ as determined by the parameters that describe the vesicle beads. While the Langevin model works well for long rods in soft vesicles where the clusters are long lived, the velocity correlation is better fit by a single exponential of the form $\exp(-t/\lambda_{\rm v})$, for most parameter values.

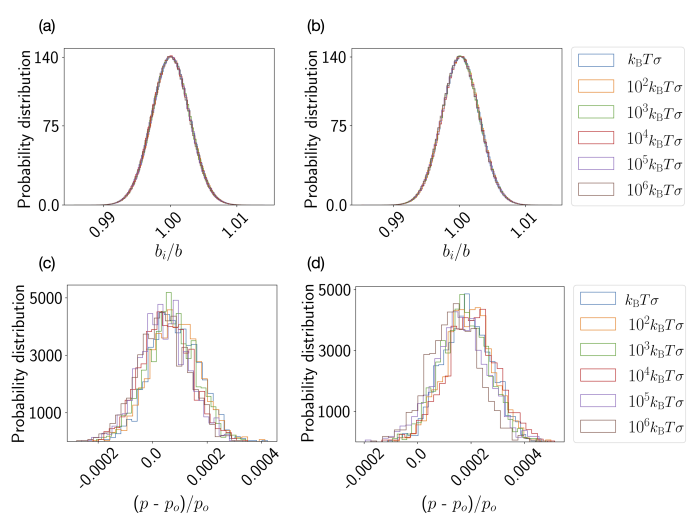


FIG. 9. Fluctuations in vesicle bond lengths and perimeter lengths are insignificant. Distributions of vesicle bead bond-lengths (a), (b) and perimeter lengths (c), (d). $b_{\rm i}$ are the measured bond lengths and $b=0.5\sigma$ is the equilibrium bond length. p is the measured perimeter and $p_{\rm o}=502.5\sigma$ is the equilibrium perimeter of the vesicle. Measurements are taken for single trial over all time steps with for $R_{\rm ves}=80\sigma$, $f_{\rm a}=3k_{\rm B}T/\sigma$, and (a), (c) $N_{\rm ves}=30$ and (b), (d) $N_{\rm ves}=100$. Coloured lines represent vesicles with different bending stiffness values.

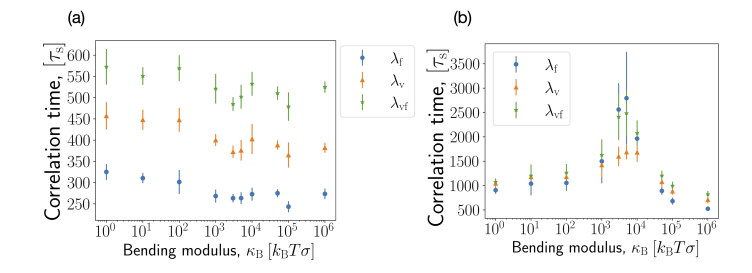


FIG. 8. Comparison of the velocity-force correlation timescale, $\lambda_{\rm vf}$ with $\lambda_{\rm v}$ and $\lambda_{\rm f}$, as a function vesicle stiffness. $\lambda_{\rm vf}$ is measured by fitting an exponential to $\langle \hat{v}_{\rm com}(t) \cdot \hat{f}_{\rm net}(t+\Delta t) \rangle = \exp\{-\Delta t/\lambda_{\rm vf}\}$. The vesicle velocity is measured by calculating the displacement of the center of mass between successive pairs of time steps. The net force is measured by summing the force imposed by the active rods on the vesicle. To enable a one-to-one comparison between force and velocity, we average the force over pairs of timesteps. Results are shown for $R_{\rm ves}=80\sigma$, $f_{\rm a}=3k_{\rm B}T$. (a) Short rods, $\ell/\sigma=3$. The three timescales are independent of vesicle stiffness. (b) Long rods, $\ell/\sigma=6$. The three time scales coincide and are enhanced at the optimal stiffness.

- [1] J. A. Anderson, J. Glaser, S. C. Glotzer, HOOMD-blue: A python package for high-performance molecular dynamics and hard particle monte carlo simulations, Computational Materials Science 173, 109363 (2020).
- [2] T. D. Nguyen, C. L. Phillips, J. A. Anderson, and S. C. Glotzer, Rigid body constraints realized in massively-parallel molecular dynamics on graphics processing units, Comput. Phys. Commun. **182**, 2307 (2011).